STUDIA UBB PHYSICA, Vol. 66 (LXVI), 1-2, 2021, pp. 91-110
(RECOMMENDED CITATION)
doi:10.24193/subbphys.2021.09

PERPENDICULAR MAGNETIC ANISOTROPY AND ITS ELECTRIC FIELD MANIPULATION IN MAGNETIC MULTILAYERED HETEROSTRUCTURES

ROXANA-ALINA ONE[1], SEVER MICAN[1], CORIOLAN VIOREL TIUSAN[1,2,3] *

ABSTRACT. Understanding of underlying physics related to the Perpendicular Magnetic Anisotropy (PMA) in magnetic heterostructures represents a major issue for its exploit in random-access memory (MRAM) devices. Using ab-initio analysis, we reveal some basic aspects related to the anatomy of PMA and its variation with electric field in various *X*/Fe/MgO(001) multilayer configurations (*X*=Cr, Au, V, Ag, Pt, Pd,…) compatible with standard experimental architectures of magnetic tunnel junction devices. Our study quantifies and underlines the significant role of the Rashba interfacial field on PMA. We explain and correlate the sign, the magnitude, and the electric field dependence of the PMA, the Rashba coefficient α_R and the Dzyaloshinskii–Moriya (DMI) asymmetric exchange interaction parameter. Moreover, when varying the Fe thickness in X/Fe/MgO(001) systems, we observe oscillations of PMA with the number of Fe monolayers, explained within the framework of quantum wells of the Δ_1 Bloch symmetry electrons in Fe. Further atomistic micromagnetic simulations including different Fe layer thicknesses and the corresponding PMA predict macroscopic magnetization characteristics in realistic experimental systems.

Keywords: *perpendicular magnetic anisotropy, electric field control of PMA, magnetic tunnel junctions, magnetic multilayer heterostructures, atomistic magnetic simulations.*

INTRODUCTION

Perpendicular Magnetic Anisotropy (PMA) in ultrathin magnetic films represents one of the most challenging topics for data storage applications, related to both high thermal stability and low switching currents in spin-transfer-torque

[1] *Babeș-Bolyai University, Faculty of Physics, 1 M. Kogălniceanu, 400084, Cluj-Napoca, Romania*
[2] *Technical University of Cluj-Napoca, Department of Physics and Chemistry, 28 Memorandumului, 400114, Cluj-Napoca, Romania*
[3] *National Center of Scientific Research, France*
* *Corresponding author: coriolan.tiusan@ubbcluj.ro*

magnetic random-access memories (MRAM). A deep understanding of fundamental underlying physics related to the PMA anatomy in magnetic multilayer structures represents a major issue for further exploit in MRAM devices [1]. The control of the interfacial magnetic anisotropy by external electric fields leads to a novel strategy for the control of the magnetization in spintronic devices with enhanced energetic efficiency [2]. Within this paradigm, energy consumption of few fJ/bit [3,4] and sub-nanosecond switching times can be achieved [5]. Despite obvious recent advances, the control of ultra-thin ferromagnetic layers magnetism by external electric field remains a complex topic with complex mechanisms simultaneously involved. It is commonly accepted that the PMA in ultrathin magnetic heterostructures has interfacial origin: proximity effects at the interfaces with non-magnetic materials with enhanced spin-orbit coupling (e.g. Pt, Au…) and intrinsic electric field and specific hybridization at interfaces with oxides (e.g. MgO). Within this last framework, an external electric field would trigger a modulation of the magnetic anisotropy via the following competing effects: (i) E-field induced surface charge doping (change of orbitals occupancy [6,7]); (ii) E-field influence on the interfacial dipole field that exists at the ferromagnetic/insulator interface even in the absence of an external magnetic field. The anisotropy energy is not located at the interface but extends towards the bulk like an attenuated wave [8]; (iii) the E-field effect on the interfacial Rashba spin-orbit coupling that affects the magnetic anisotropy energy via a Dzyaloshinskii-Moriya mechanism [9]; (iv) E-field induced ion migration [10]. Within this still open fundamental topic one can argue that the electric field control of the anisotropy is driven by collective mechanisms and that a better understanding of the underlying physics could lead to an enhancement of potential capabilities for energetically efficient magnetization manipulation in spintronic devices.

In this study we involve ab-initio analysis and atomistic magnetic calculations to unveil some basic aspects related to the anatomy of PMA and its variation with electric field in *X*/Fe/MgO(001) multilayer configurations (*X*=Cr, Au, V, Pd, Pt, Ag…) compatible with standard experimental architectures of magnetic tunnel junction devices. Moreover, our study quantifies and underlines the significant role of the Rashba interfacial field on PMA, explaining and correlating the sign, the magnitude, and the E-field dependence of the PMA, the Rashba coefficient α_R and the Dzyaloshinskii–Moriya (DMI) asymmetric exchange interaction parameter. In *X*/Fe/MgO(001) systems with a variable Fe thickness we illustrate oscillations of PMA with the number of the Fe monolayers related to quantum well effects. Based on electronic structure characteristics extracted from the ab-initio calculations, we performed atomistic micromagnetic simulations to predict macroscopic magnetization characteristics corresponding to nanostructures with different Fe thicknesses and related PMA amplitudes.

THEORETICAL DETAILS

The theoretical study of the PMA and its field control has been performed using the ab-initio *Full Potential Linear Augmented Plane Wave FP-LAPW* code *Wien2k* [11]. In our calculations we involved a super-cell model thoroughly chosen to describe the *X*/Fe/MgO(001) multilayer configuration.

Magnetic anisotropy calculations in Wien2k

The magnetic anisotropy energy (MAE) has been calculated within a fully relativistic spin orbit scheme using total energy and force theorem approaches [12], both providing similar results. Within the total energy approach, the MAE is calculated as the difference between the total energy *E*[*uvw*] deduced from spin orbit calculation with the magnetization along the [*uvw*] crystallographic direction and the total energy corresponding to the magnetization along the easy axis:

$$MAE = E[uvw] - E[easy\ axis]$$

The force theorem approach is a perturbative formalism in which the MAE between two different magnetization directions $\vec{m}_1$ and $\vec{m}_2$ is given by:

$$MAE = \sum_{i,k}^{occ} \varepsilon_i^1(\vec{m}_1, k) - \sum_{i,k}^{occ} \varepsilon_i^1(\vec{m}_2, k)$$

where the superscript 1 denotes the band energies calculated using the fully relativistic charge/spin density of magnetization $\vec{m}_1$.

Spin-orbit coupling in Wien2k

The quantum mechanics description of electrons, consistent with the theory of special relativity is provided by the Dirac equation: $H_D\Psi = \varepsilon\Psi$, where H_D is the Dirac Hamiltonian: $H_D = c\vec{\alpha}\cdot\vec{p} + \beta mc^2 + V$.
$\alpha_k = \begin{pmatrix} 0 & \sigma_k \\ \sigma_k & 0 \end{pmatrix}$, $\beta_k = \begin{pmatrix} 1 & 0 \\ 0 & -1 \end{pmatrix}$ and σ_k are the Pauli matrices: with: $\sigma_x = \begin{pmatrix} 0 & 1 \\ 1 & 0 \end{pmatrix}, \sigma_y = \begin{pmatrix} 0 & -i \\ i & 0 \end{pmatrix}$, $\sigma_z = \begin{pmatrix} 1 & 0 \\ 0 & -1 \end{pmatrix}$. H_D and the wave function are 4-dimensional objects. Within the non-relativistic limit of the Dirac equation the electrons are moving with velocities much smaller than the speed of light. Some

relativistic effects can be neglected, and they can be described by the Pauli equation which considers the interaction of the particle spin with an external electromagnetic field. The corresponding Pauli Hamiltonian can be written as:

$$H_P = -\frac{\hbar}{2m_0}\nabla^2 + V_{eff} + \mu_B \vec{\sigma} \cdot \vec{B}_{eff} + \xi\left(\vec{\sigma} \cdot \vec{l}\right)$$

The first term is the kinetic term in the Schrödinger equation, the second term is an electrostatic effective potential, the third term is a Stoner term describing the Zeeman interaction of the spin with an external effective magnetic field and the fourth term the spin-orbit coupling term. $\vec{\sigma}$ is the Pauli matrices vector $\vec{\sigma} = \left(\sigma_x, \sigma_y, \sigma_z\right)$ and ξ is the constant of the spin-orbit interaction. The matrix of the Pauli Hamiltonian is 2x2 in the spin space. Due to the Pauli spin operators the wave function is a 2-component vector (spinor), each component $\Psi_{1(2)}$ being associated to a spin orientation 1=up, 2=down): $H_P \begin{pmatrix} \Psi_1 \\ \Psi_2 \end{pmatrix} = \varepsilon \begin{pmatrix} \Psi_1 \\ \Psi_2 \end{pmatrix}$.

The effective potential is a sum of an external potential, an electrostatic Hartree term and an exchange-correlation potential: $V_{eff} = V_{ext} + V_H + V_{xc}$. The effective magnetic field is composed by an external field and an exchange correlation field: $B_{eff} = B_{ext} + B_{xc}$. Both exchange correlation potential V_{xc} and magnetic field B_{xc} are defined within the Density functional Theory (DFT) in either Local Density Approximation (LDA) or Generalized Gradient Approximation (GGA).

Exchange and correlation

From the DFT LDA exchange-correlation energy defined as an integral of the exchange-correlation energy ϵ_{xc} per particle of a homogeneous electron gas of electronic charge density *n(**r**)* and spin density $\vec{m}(\boldsymbol{r})$:

$E_{xc}(n, \vec{m}) = \int n\epsilon_{xc}(n, \vec{m})dr^3$ one can calculate V_{xc} and B_{xc} as functional derivatives: $V_{xc} = \frac{\partial E_{xc}(n,\vec{m})}{\partial n}$ and $\vec{B}_{xc} = \frac{\partial E_{xc}(n,\vec{m})}{\partial \vec{m}}$. Within the LDA approach we get: $V_{xc} = \epsilon_{xc}(n, \vec{m}) + n\frac{\partial \epsilon_{xc}(n,\vec{m})}{\partial n}$ and $\vec{B}_{xc} = n\frac{\partial \epsilon_{xc}(n,\vec{m})}{\partial \vec{m}}\hat{m}$ with $\vec{B}_{xc}$ parallel with $\hat{m}$.

Relativistic effects in Wien2k

In Wien2k the relativistic effects are included inside of the muffin-tin atomic spheres where the potential has a spherical symmetry leading to relativistic

equations in a spherical atomic geometry. Therefore, different types of electrons are differently treated, as follows:

(i) *The core electrons* within the atomic sphere region are "fully" relativistic, the core states are fully occupied and obey the spin-compensated Dirac equation in a spherical potential that include the SOC.

$$\left[-\frac{\hbar}{2m_0}\nabla^2 + V_{eff} + \mu_B\vec{\sigma}\cdot\vec{B}_{eff} - \frac{p^4}{8{m_0}^3c^2} - \frac{\hbar^2}{4{m_0}^2c^2}\frac{dV}{dr}\frac{\partial}{\partial\vec{r}} + \frac{1}{2{m_0}^2c^2}\frac{1}{r}\frac{dV}{dr}\left(\vec{l}\cdot\vec{s}\right)\right]\Phi = \varepsilon\Phi$$

First and second term give non-relativistic Schrödinger equation. The third term is a Stoner or Zeeman correction describing the interaction with an external magnetic field. Fourth and fifth terms are mass and Darwin relativistic correction, respectively. The last term corresponds to the spin-orbit coupling (SOC). For spin-polarized potential, spin up and spin down are calculated separately, the density is averaged according to the occupation number. The SOC mixes up and down states, $j = l + s$ is a good quantum number.

(ii) *The valence electrons* inside the atomic muffin-tin spheres are treated with scalar-relativistic approximation. All relativistic effects are included except the SOC that can be further included in «second variation».

(iii) *The valence electrons* belonging to the interstitial region are treated as non-relativistic.

Computational issues

Having in view the extreme sensitivity of the magnetic anisotropy energy to the *k*-space meshing, first, the convergence of the total energy with respect to the total number of *k*-points has been thoroughly performed. Within the total energy approach, using spin-orbit calculation, the perpendicular magnetic anisotropy (PMA) has been calculated as the total energy difference between the configurations where the magnetization was set along perpendicular to the film's plane and in-plane directions. The perturbative formalism of the force theorem approach provides the MAE from the band energies calculated using the fully relativistic charge and spin density of magnetizations corresponding to two distinct directions. Within these formalisms, the electric field (E-field) has been applied using a zig-zag additional potential in the Hamiltonian, as implemented by Stahn et al [13]. Therefore, for different values of electric field, the MAE can be calculated to provide theoretical

insight on its electric field dependence. Quantitatively, the response of the PMA with respect to applied external electric field has been further described in terms of the β coefficient, defined as the slope of the variation of the surface perpendicular anisotropy K_s with the electric field *E*, felt by the ferromagnetic ultrathin film.

Calculation of the Rashba parameter α_R from Wien2k band structure

The spin-orbit term of the non-relativistic Dirac (Pauli) Hamiltonian: $H_{SO} = \frac{\hbar}{(2m_0c)^2}\vec{\nabla}V \cdot (\vec{\sigma} \times \vec{p})$ can be simplified for 2 dimensional electronic systems with the confinement direction (e.g. *Oz* in a Cartesian system) perpendicular to the propagation direction (within the *xOy* plane) leading to the Rashba Hamiltonian: $H_R = \alpha_R \vec{\sigma}(\vec{k} \times \vec{e}_z)$ where $\alpha_R = \frac{\hbar^2}{(2m_0c)^2}\frac{\partial V}{\partial z}$ is the Rashba constant which is a measure of the spin-orbit interaction and $\vec{e}_z$ the unit vector of the *Oz* (electron confinement) direction. From its definition, one can see that α_R is proportional with the electric field $E = -\frac{\partial V}{\partial z}$ aligned along the *Oz* direction. We will see later that in a multilayer stack, at the interface between two different materials, such kind of electric fields naturally exist and lead to Rashba spin-orbit interaction effects. The SO-coupling is exacerbated at the metal surfaces: the breaking of the translational symmetry in surface is equivalent to a potential gradient felt by the electron. In the case when a metal-insulator (or metal semiconductor) interface is created in a multilayer heterostructure, a depletion zone appears with a corresponding significant interfacial electric field. By diagonalizing the Rashba Hamiltonian, the eigenvalues will be:

$$E_{\pm}(k_{II}) = \frac{\hbar^2 k_{II}^2}{2m_0} \pm \alpha_R |k_{II}|$$

representing parabolic bands with an offset of the parabola minimum in positive (or negative) *k* values (Rashba splitting). The minimum of the parabola can be found as $\frac{\partial E}{\partial k} = 0 \Rightarrow k_0 = \frac{m_0 \alpha_R}{\hbar^2}$ so that $E_{\min} = E_0 = \frac{\hbar^2 {k_0}^2}{2m_0}$ that leads to $E_0 = \frac{k_0 \alpha_R}{2}$. From this equation wee see that α_R can be calculated when knowing the values of *E* and *k* corresponding to the minimum of the parabolic dispersion band: $\alpha_R = \frac{2E_0}{k_0}$. As we will see in the section related to results, we have used this equation to extract the Rashba parameter from the Rashba offset of the parabolic bands calculated for different supercell models describing our magnetic multilayer heterostructures. Experimentally, the spin-orbit constant α_R can be extracted from ARPES (Angular Resolved Photoemission) [14,15].

Atomistic calculations

The results issued from the ab-initio calculations, e.g., atom projected magnetic moments, PMA, DMI, have been used as input parameters for atomistic calculations performed within the framework of the atomistic code *VAMPIRE* [16]. The main input files for running the atomistic code contain information about materials and properties that enter in the sample composition: sandwiches of magnetic or nonmagnetic materials, alloys, etc. and system configurations: dimensions, simulation described in detail with all the necessary parameters (atomic positions with the exchange matrix components and type of exchange (isotropic, vectorial, tensorial). Within the atomistic magnetic calculation approach implemented in *VAMPIRE* the atoms have been considered as individual interacting entities with a given magnetic moment. Similarly to the macroscopic LLG approach, the spin dynamics is obtained by integrating the Landau–Lifshitz-Gilbert (LLG) equation applied at the atomistic level for the atomic spins. Here, the atomistic LLG equation:

$$\frac{\partial \vec{\boldsymbol{S}}_i}{\partial t} = -\frac{\gamma}{(1+\lambda^2)}\left[\vec{\boldsymbol{S}}_i \times \vec{H}^i_{eff} + \lambda \vec{\boldsymbol{S}}_i \times (\vec{\boldsymbol{S}}_i \times \vec{H}^i_{eff})\right]$$

describes the interaction of an atomic spin moment $\vec{\boldsymbol{S}}_i$ with an effective magnetic field $\vec{H}^i_{eff}$ of each spin *i* derived from the complete spin Hamiltonian $\mathcal{H}$ including all the interaction and anisotropy terms describing the modeled system (e.g., exchange, anisotropy, Zeeman interaction with external applied fields):

$$\mathcal{H} = \mathcal{H}_{exc} + \mathcal{H}_{ani} + \mathcal{H}_{app}; \qquad \vec{H}^i_{eff} = -\frac{1}{\mu_S}\frac{\partial \mathcal{H}}{\partial \vec{\boldsymbol{S}}_i}$$

where μ_S is the local spin moment, γ is the absolute value of the gyromagnetic ratio, λ the microscopic Gilbert damping parameter. The effect of the temperature has been included using the Langevin dynamics [17] assuming that the thermal fluctuations on each atomic site can be represented by a Gaussian white noise term $\Gamma(t)$ whose width is proportional with the temperature value. The corresponding thermal field will be: $H^i_{th} = \Gamma(t)\sqrt{\frac{2\lambda k_B T}{\gamma \mu_S \Delta T}}$, where k_B is the Boltzmann constant and *T* is the temperature of the system. To determine the time dynamics of systems of spins, the stochastic LLG equation is solved numerically (integrated) within the Heun predictor corrector scheme.

In this paper, the simulations have been performed for cylindrical Au/Fe/MgO multilayer nanostructures with a diameter of 15 nm (the integration range of the LLG equations). Periodic boundary conditions (PBC) have been included to calculate magnetic properties of macroscopically large magnetic heterostructure systems. As input for the *VAMPIRE* code, we have used thickness dependent PMA and atom resolved magnetic moments extracted from *Wien2k* ab-initio calculations performed on super-cell models describing the realistic Au/Fe/MgO(001) systems with variable Fe thicknesses.

RESULTS AND DISCUSSION

Ab-initio calculations

A typical supercell model used in our ab-initio calculations is depicted in fig. 1. As we mentioned, in the calculation the electric field can be introduced via a zig-zag potential term in the Hamiltonian. Following the zig-zag potential E-field implementation within the Wien2k code by Stahn et al [13], the supercell contains the multilayer sequence in half of its volume, the other half being a vacuum region. Therefore, a constant *E*-field equal to $-\Delta V/\Delta z$ will be localized at the Fe/MgO interface, the amplitude and sign of the electric field being driven by the *V* ramp amplitude and the choice of an ascending or descending *V* ramp in that region. The *k*-space mesh used in our calculation was $25\times25\times1$, which resulted from a preliminary study of the total energy convergence with respect to the total number of *k*-points in the Brillouin zone. Having in view the sensitivity of the MAE to energy development parameters in *Wien2k*, especially when including relativistic local orbitals (LAPW+l_0), we set E_{max}=100, meaning that all scalar relativistic eigenstates are included when the spin-orbit-coupling is switched on. The size of the basis set used in the expansion of the wave function was $R \cdot K_{max}$=7, where *R* is the smallest atomic muffin-tin sphere radius, R_{MT}, times the largest *K*-vector, K_{max}.

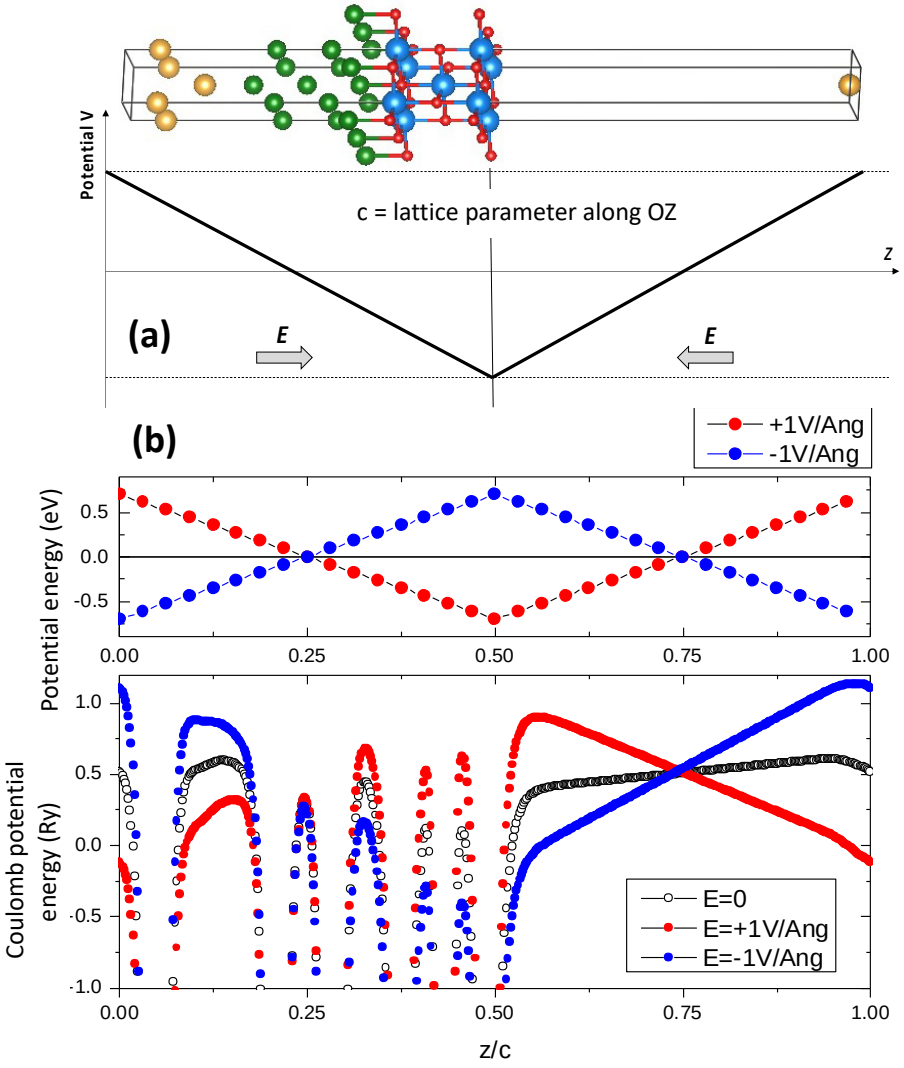

Fig. 1. (a) Supercell model used to describe the *X*/Fe/MgO(001) system; here the thickness of Fe is 5 monolayers (ML). Zig-zag potential leading to a constant $\vec{E} = -\nabla V = -\frac{dV}{dz}\vec{e}_z$ in the half of the supercell where the *X*/MgO interface is placed. The sign of the applied electric field is determined by the sign of the chosen ramp slope; (b) Potential energy corresponding to the ramp potential and self-consistently calculated Coulomb potential on each atom in the supercell.

Having in view the complexity of the problem, the computational tasks have been performed within a *k*-point parallelization scheme using a 48-CPU workstation. From the ab-initio calculations, for various *X*/Fe/MgO configurations, we obtained the following main results, synthetized in table 1:

Table 1. Calculated magnetic anisotropy energy (MAE) for various multilayer heterostructure systems in which the ultrathin Fe is sandwiched between *X* and MgO with *X* = V, Au, Pd, Ag, MgO, Pt. The number represents the # of monolayers. The slope of the MCA variation with applied electric field is β. We also indicate the lattice parameters used in the ab-initio calculations.

System	MAE (V=0) E_{perp}-E_{plan}	MAE (V=0)	β	a=b	Crystallographic phase
	meV	erg/cm^2= mJ/m^2	fJ/Vm	Å	
V3/Fe5/MgO-vid	0.54	0.94	68.44	3.02996	cubic (100)
Au3/Fe5/MgO-vid	0.71	1.37	-32.26	2.883162	cubic (100)
Au3/Fe5-Pt1/MgO-vid	5.86	11.28	-56.65	2.883162	cubic (100)
Pd3/Fe5/MgO-vid	0.43	0.83	17.3	2.883162	cubic (100)
Pd3/Fe5-Pt1/MgO-vid	5.13	9.87	87.46	2.883162	cubic (100)
Ag3/Fe5/MgO-vid	1.35	2.59	-	2.888263	cubic (100)
MgO/Fe3-MgO-vid	1.91	3.71	-	2.8689	cubic (100)
Pt3/Co5/MgO-ot-aPt-vid	0.23	0.58	-43.43	2.7709	hexa (111)

(i) The calculated systems mostly present perpendicular magnetic anisotropy, i.e., the most stable configuration corresponds to the magnetization being aligned along the *z*-direction. However, for some systems: Cr3/Fe5/MgO(001), Pt3(001)/Fe5/MgO, Pt3(111)/Co5/MgO, the ground state corresponds to a configuration in which the magnetization lies in-plane.

(ii) The perpendicular anisotropy can be significantly enhanced if one monolayer of Pt is inserted at the top interface, between Fe and MgO. Moreover, the adjunction of the top Pt layer changes the response of the PMA with respect to an external applied electric field.

(iii) The electric field response of the PMA is specific for each system. One can tailor the amplitude and the sign of the variation by changing the chemical nature of the bottom interface *X*/Fe (fig. 2).

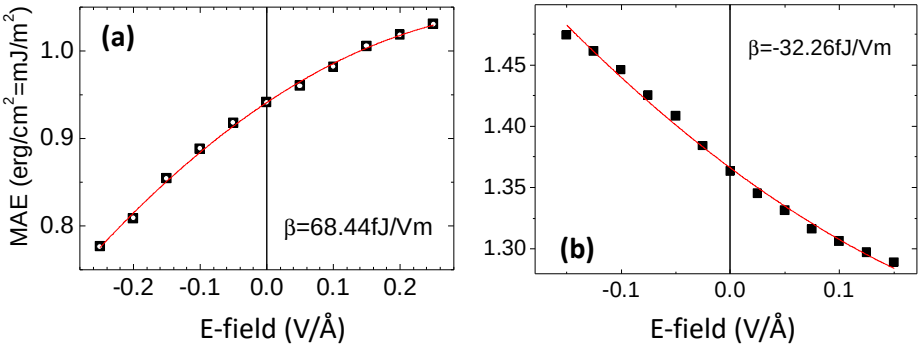

Fig. 2. Magnetic anisotropy energy dependence on electric field (E-field) for (a) V3/Fe5/MgO and (b) Au3/Fe5/MgO systems. Open circles in (a) correspond to Force theorem, black squares to total energy MAE calculations. The sign of the variation slope is different, indicating the significant role of the bottom *X*/Fe interface (*X*=V, Au) on the PMA and its field variation.

The opposite sign variation of the PMA with the E-field can be explained by considering the Rashba field at the bottom *X*/Fe interface whose sign depends on the relative work-functions of Fe and *X* metals (see fig. 3), as theoretically predicted by Barnes et al [9]. The effect of an external electric field on the intrinsic fields $E_1 = E_T$ ($E_2 = E_B$) at the top (bottom) interfaces is illustrated in fig. 4, the analysis being performed for Au/Fe/MgO system.

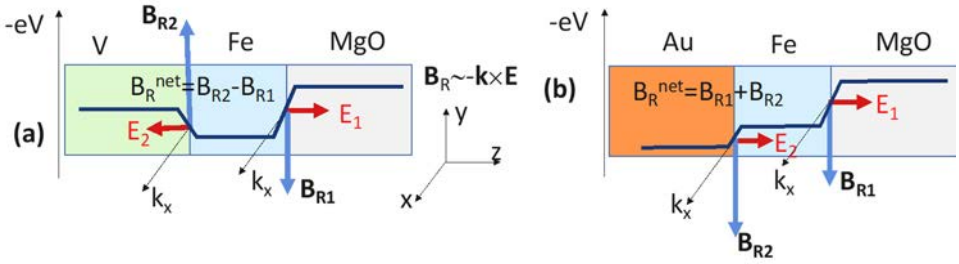

Fig. 3. Potential profiles, Rashba fields B_R related to the intrinsic electric fields at the top (1)=Fe/MgO and the bottom (2)=*X*/MgO interfaces in (a) V3/Fe5/MgO and (b) Au3/Fe5/MgO systems. In (a), $E_{ext} < 0$ decreases E_1 (so B_{R1}) => B_R^{net} (and α) increases. In (b) $E_{ext} < 0$ decreases E_1 (so B_{R1}) => B_R^{net} (and α) decreases.

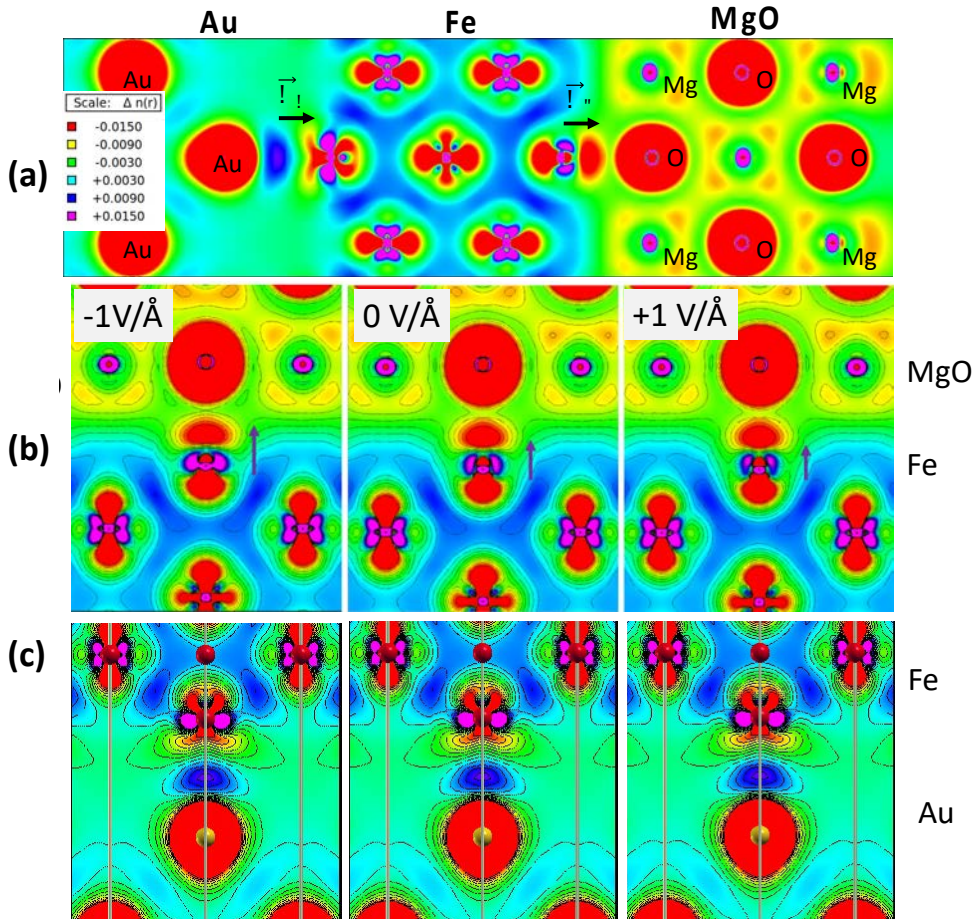

Fig. 4. Valence charge density plots for the Au3/Fe5/MgO stack: (a) complete stack, (b) zoom at the top Fe/MgO and (c) bottom Au/MgO interfaces illustrating the effect of an external electric field on the interface intrinsic fields E_1 (top) and E_2 (bottom).

As expected, we clearly illustrate that the external electric field only influences the top interface, being completely screened at the metallic bottom Au/Fe interface (no field effect observed, fig. 4(c)). The variation of the electric field E_1 at the top interface Fe/MgO when an external field is applied can be directly correlated to the charge and magnetic moment variation for the interface Fe(/MgO) atom, issued from the ab-initio calculation and illustrated in fig. 5. We see from the analysis depicted in fig. 5 that a positive external electric field increases the charge

on the interface Fe atom (the depletion decreases) and this corresponds to a decrease of the Fe magnetic moment, as expected for its "roughly" $3d^6$ configuration. From the Rashba splitting of the band structure corresponding to opposite orientations of the magnetization with respect to the crystallographic axes (directions with **k**⊥**M**) we calculated the Rashba parameter α_R (see fig. 6): $\alpha_R = \frac{2E_0}{k_0}$ where E_0 corresponds to the minimum of the parabolic dispersion and k_0 the corresponding wave vector where *E(k)* has a local minimum.

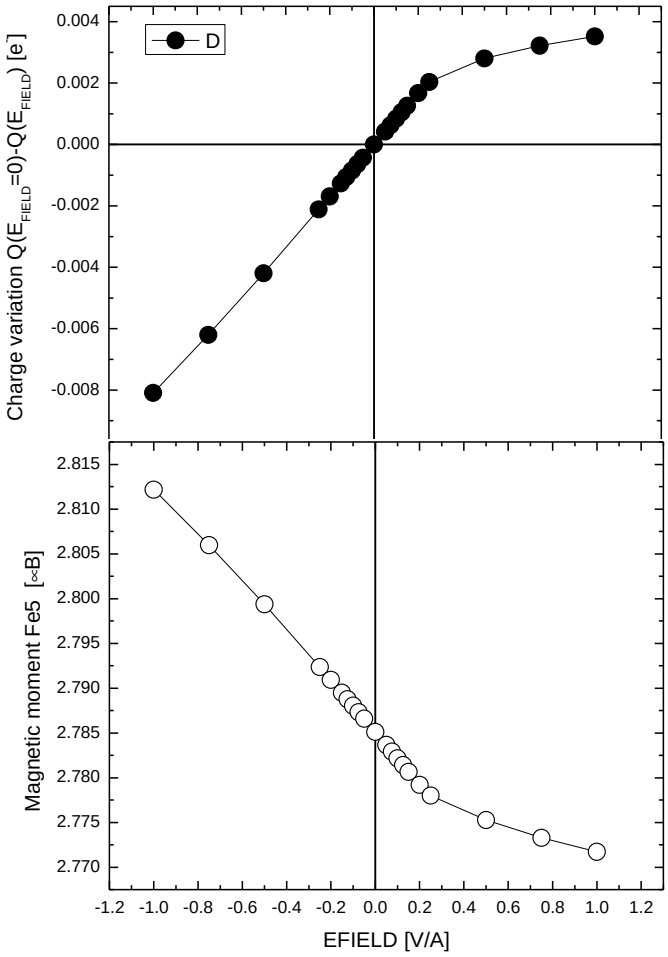

Fig. 5. Charge variation within the muffin-tin sphere of the interface Fe(/MgO) atom (top panel) and corresponding magnetic moment with respect to the external applied electric field (Volt/Angstrom units).

In this way, we demonstrate that opposite sign Rashba parameters can be obtained in V/Fe/MgO and Au/Fe/MgO systems, corresponding to opposite Rashba offset in *k* of the surface Fe parabolic bands in the *X*/Fe/MgO stack, where *X*=V and Au (fig. 6). While the top interface Fe/MgO is identical in the two configurations, it is obvious that the opposite offset sign is related to the bottom interface, demonstrating the major influence of the Rashba fields at both top and bottom interfaces on the PMA and the net α_R.

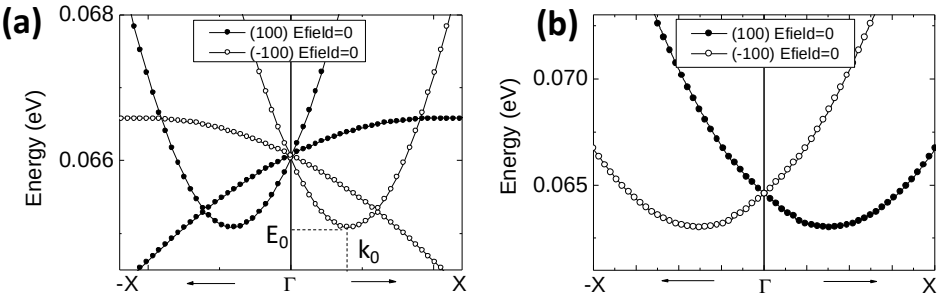

Fig. 6. Parabolic band dispersion of surface bands of Fe in *X*/Fe5ML/MgO system, where *X*=V (a) and X=Au (b). The bands corresponding to the magnetization *M* parallel to (100) and (-100) are oppositely shifted in *k* due to the net Rashba field whose sign is determined by both bottom *X*/Fe and top Fe/MgO interfaces (see explanation related to fig. 3). $E_{\min} = E_0 = \frac{\hbar^2 {k_0}^2}{2m_0}$.

This illustrates that the bottom interface Rashba magnetic field B_{R2} has a long-range influence and, by its sign and amplitude, can modulate the net Rashba field in the stack (see fig. 3).

(iv) Within the framework of a still under debate issue in the literature, in which the asymmetric exchange Dzyaloshinskii-Moriya interaction can be triggered by a Rashba mechanism [18], we calculated the DMI constant from the Rashba splitting and the Rashba constant α_R: $DMI = 2k_R A$, where *A* is the Fe exchange stiffness (21 pJ/m [19]), $k_R[\text{Å}^{-1}] = 0.2619 * \alpha_R[eV\text{Å}]\, m_e$, m_e is the effective mass of the electrons in Fe, estimated to be equal to 0.57 from the fit of the parabolic bands illustrated in fig. 6(b) - corresponding to Au/Fe/MgO system. Using this algorithm, we calculated, explained and correlated the sign, the magnitude and the electric field dependence of the PMA, the Rashba coefficient α_R and the Dzyaloshinskii–Moriya (DMI) asymmetric exchange interaction parameter in different *X*/Fe/MgO(001) systems (see example in fig. 7 for Au/Fe/MgO system). It is important to mention

that the sign of the DMI, correlated to the sign of the Rashba parameter, has a significant importance in magnetic heterostructures: It determines the topological charge of chiral structures (domain walls and skyrmions) and the direction of their velocity when manipulated by spin transfer torques related to spin currents in emerging generation of race-track memories [20, 21]. Therefore, a major issue of our calculations is related to the prediction of an original strategy for the DMI sign, amplitude, and E-field control via the interface engineering in experimental magnetic multilayered stacks.

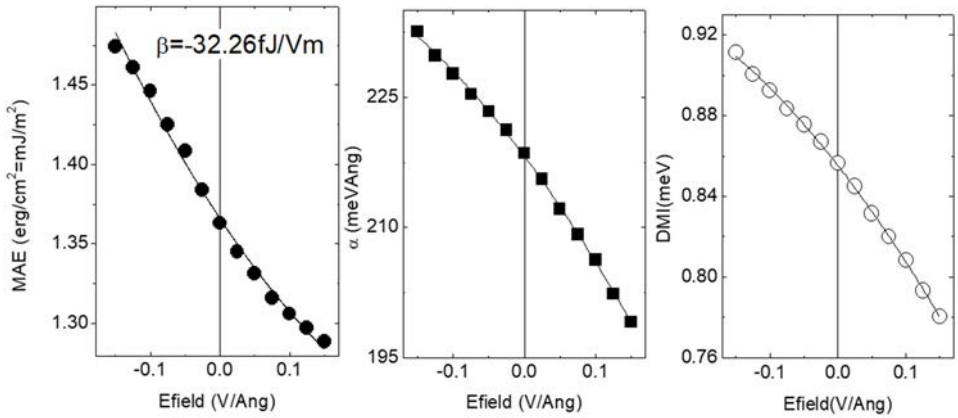

Fig. 7. Typical curves of electric field dependence of PMA, α_R and DMI in the Au/Fe(5ML)/MgO system.

(v) When varying the Fe thickness in X/Fe/MgO(001) systems, with *X*=V, Cr, Au, we observe clear oscillations of PMA with the number of the Fe monolayers (fig. 8).

We explained these oscillations within the framework of quantum wells of the Δ_1 Bloch symmetry Fe electrons, as we previously demonstrated in spin dependent transport experiments in Fe/Cr/Fe/MgO single crystal MTJs [22], where similar quantum well effects and oscillation period of the tunnel conductance has been observed. The predicted PMA oscillations with the ferromagnetic layer thickness represent a major issue for understanding the PMA and the DMI in realistic experimental system with sizable roughness and thickness fluctuations, even at an atomic level. In a first step, in this work, we performed atomistic micromagnetic calculations of magnetic properties (hysteresis curves) of Au/Fe(*t*)/MgO nanostructures with a variable thickness *t* = 3, 4, 5 ML both at 0 K and room temperature.

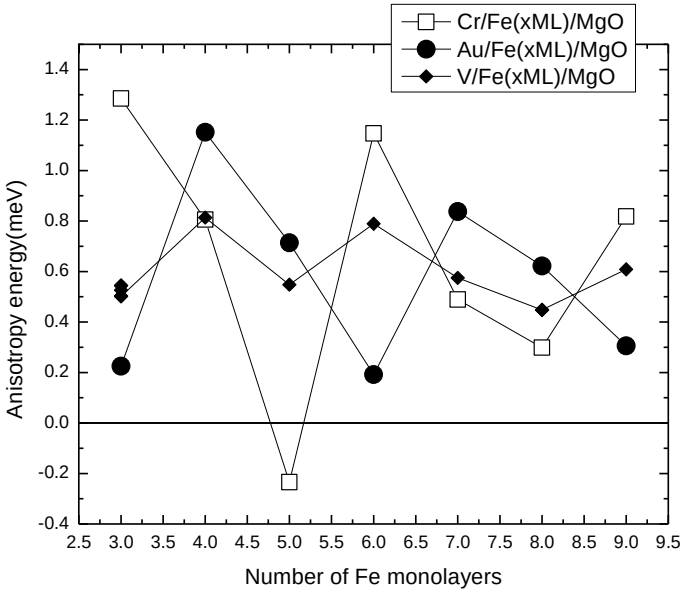

Fig. 8. Magnetic anisotropy energy for X/Fe/MgO(001) slabs where *X*=Cr(001), Au(001), V(001), extracted from ab-initio calculations. Positive (negative) MAE correspond to perpendicular (in-plane) magnetization (PMA) configurations.

Atomistic simulations for Au/Fe/MgO system modelled as flat terraces

In order to extend the theoretical analysis of the Au/Fe/MgO system to larger dimensions, we chose to simulate a layered structure in the atomistic framework. Following this approach, we can represent with high fidelity the case of MBE terraces and, in addition, we can benefit from the time and resources efficiency that this numerical tool provides us with.

Three samples were modelled as flat slabs of constant thickness, with periodic boundary conditions – Table 2. The hysteresis loops have been simulated with a field applied along the *Oz* direction. By doing so, we avoid the well-known computational expenses of working with a tremendously large number of dipole field cubic macrocells, but we can still use the smallest macrocell size for a high precision dipole field calculation. The input parameters such as the layer resolved magnetic moments per atom and anisotropy constants were obtained from the first principles method. A convergence study at T = 0 K was performed in order to establish the suitable simulation parameters of the hysteresis loops, in agreement with the Stoner-Wohlfarth model.

For *T*=0 K, without considering the dipole field, all of the samples display rectangular hysteresis loops with coercivities in perfect agreement with the Stoner Wohlfarth model, as represented in Table 2. If we add the dipole field to our model, only the 4ML and 5ML samples preserve their coercivity, as the 3ML sample magnetization becomes tilted in-plane. It can be observed that the coercive field varies with the thickness in a similar fashion as the anisotropy energy. Also, it is worth mentioning that the rectangular shape of the hysteresis loops is the evidence of a perpendicular magnetization orientation. This is a numerical confirmation that can be verified experimentally in a range of ultra-low temperatures, where the effect of thermal fluctuations is diminished.

Table 2. Coercive field values determined analytically and from atomistic simulations at 0 K for the investigated samples.

Sample name/ no. atomic layers	**Thickness (nm)**	**Hc Stoner-Wohlfarth (*T*=0K) limit (T)**	**Hc atomistic with dipole field (*T*=0 K) (T)**
3ML / 3 atomic layers	0.429	0.99	In-plane oriented
4ML/ 4 atomic layers	0.572	3.88	1.76
5ML/ 5 atomic layers	0.715	1.95	0.10

When thermal fluctuations are added to the system, the dipolar and the thermal field compete with the anisotropy and in some situations, they will tilt the magnetization orientation from an out-of-plane to an in-plane configuration. Such a case is depicted in fig. 9, where hysteresis loops simulated at room temperature for different sample thicknesses are shown. At *T* = 300 K one can observe that the perpendicular magnetic anisotropy is strongly dependent on the thickness. For 3ML and 5ML it can be observed that the magnetization adopts an in-plane orientation, while for the 4ML thickness it is oriented perpendicular to the film plane. The effect of the thermal fluctuations can be observed in the coercivity.

The addition of the dipole field leads to lower coercive field values compared to the ones predicted by the Stoner-Wohlfarth model. Also, the thermal fluctuations have been observed to contribute to this effect. We mention that the magnetic behavior illustrated in fig. 9 follows the variation of the PMA with the thickness issued from the ab-initio calculations (see fig. 8) where a local maximum in PMA was found for 4ML of Fe.

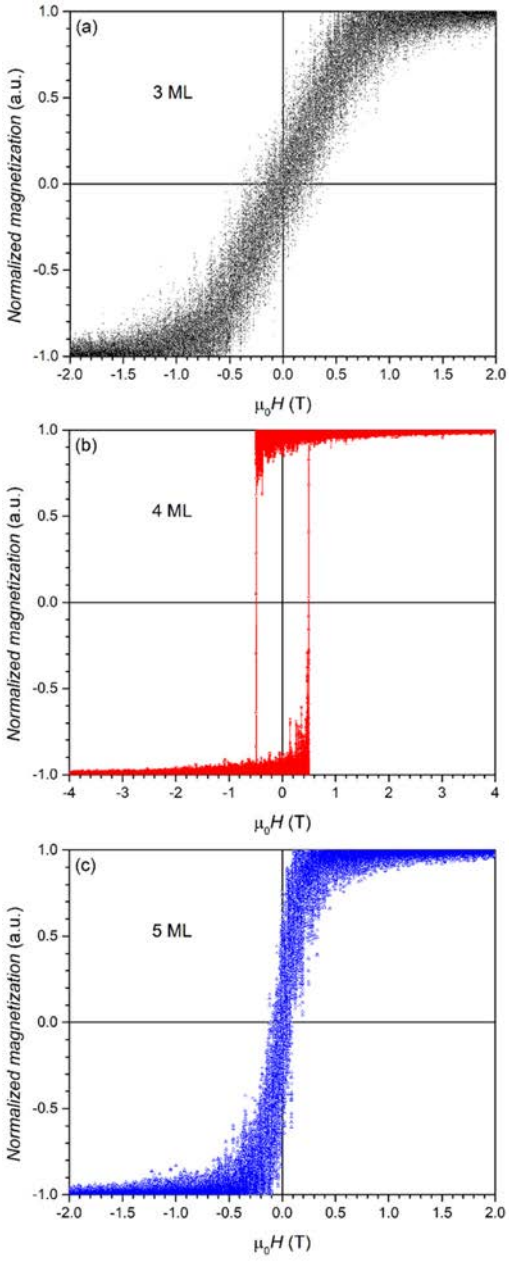

Fig. 9. Hysteresis loops at *T*=300 K obtained from atomistic simulations: (a) 3ML; (b) 4ML; (c) 5ML.

The results of our atomistic magnetic simulation indicate that to design experimental devices based on the Au/Fe/MgO system suitable for room temperature applications related to PMA one must optimize the deposition process to obtain a ferromagnetic thickness around 4ML (0.572 nm). A further coming study will consider the effect of thickness fluctuation to approach the realistic situation of experimental samples.

CONCLUSIONS

Using ab-initio calculations we have investigated some major mechanisms related to the perpendicular magnetic anisotropy and its variation with external magnetic fields. Our calculation addresses multilayer stacks with ultrathin ferromagnetic layers sandwiched between a bottom non-magnetic metal and a top MgO insulator, as commonly found in magnetic tunnel junction architectures. We point out the major contribution of the Rashba mechanism, related to interfacial intrinsic electric fields, on both PMA and DMI and underline the possibility to tailor these properties via some interfacial engineering. In this way one can tune the magnitude and the voltage response of the PMA and the sign and the magnitude of the DMI, major requests in storage and synaptic devices based on magnetic chiral structures (domain walls and skyrmions). Oscillations of the PMA with the thickness of the ferromagnetic materials have been also predicted and correlated to quantum well effects already observed by our team in spin polarized transport in Cr/Fe/MgO/Fe magnetic tunnel junctions. Finally, using atomistic magnetic simulations we have calculated macroscopic magnetic properties in Au/Fe/MgO nanostructures as a first step towards the understanding of magnetic characteristics of realistic experimental system with sizable roughness and thickness fluctuations, even at atomic level.

ACKNOWLEDGEMENTS

C.T. acknowledges funding from the project «MODESKY» ID PN-III-P4-ID-PCE-2020-0230, No. UEFISCDI:PCE 4/04.01.2021 and is grateful to M. Chshiev for fruitful discussions about PMA and the E-field manipulation anatomy. Moreover, the implementation of the current research further confirms and sustains the durability of previous funding projects: «SPINTRONIC» POS CCE Project: ID. 574, cod SMIS-CSNR 12467, «SPINTAIL» ID PN-II-PCE-2012-4-0315, No. UEFISCDI:23/29.08.2013 and «EMERSPIN» ID PN-III-P4-ID-PCE-2016-0143, No. UEFISCDI:22/12.07.2017.

REFERENCES

1. B. Dieny, M. Chshiev, *Rev. of Mod. Phys.,* vol. 89, (2017).
2. D. C. M. Yamanouchi, F. Matsukura, H. Ohno, *Science*, 301, 943-945 (2003).
3. S. Kanai, F. Matsukura, H. Ohno, *Appl. Phys. Lett.*, 108, 192406 (2016).
4. C. Grezes, F. Ebrahimi, J. G. Alzate, X. Cai, J. A. Katine, J. Langer, B. Ocker, P. Khalili Amiri, K. L. Wang, *Appl. Phys. Lett.,* 108, 012403 (2016).
5. E. G. V. Krizakova, G. Sala, F. Yasin, S. Couet, G. S. Kar, K. Garello, P. Gambardella, *Nature Nanotechnology*, 15, 111 (2020).
6. M. K. Niranjan, C-G. Duan, S. S. Jaswal, E. Y. Tsymbal, *Appl. Phys. Lett.,* 96, 222504 (2010).
7. K. H. He, J. S. Chen, Y. P. Feng, *Appl. Phys. Lett.*, 99, 072503 (2011).
8. F. Ibrahim, H. Yang, A. Halla, M. Chshiev, *Phys. Rev. B*, 93, 014429 (2016).
9. S. E. Barnes, J. Ieda, S. Maekawa, *Sci. Rep.*, 4, 4105 (2015).
10. T. Srivastava, M. Schott, R. Juge, V. Křižáková, M. Belmeguenai, Y. Roussigné, A. Bernand-Mantel, L. Ranno, S. Pizzini, S-M. Chérif, A. Stashkevich, S. Auffret, O. Boulle, G. Gaudin, M. Chshiev, C. Baraduc, H. Béa, *Nano Lett.*, 18, 4871 (2018).
11. P. Blaha, K. Schwarz, F. Tran, R. Laskowski, G. K. H. Madsen, L. D. Marks, *J. Chem. Phys*., 152, 074101 (2020).
12. X. Wang, D-S. Wang, R. Wu, A.J. Freeman, *J. Magn. Magn. Mater.*, 159, 337 (1996).
13. J. Stahn, U. Pietsch, P. Blaha, and K. Schwarz, *Phys. Rev. B*, 63, 165205, (2001).
14. G. Nicolay, F. Reinert, S. Hufner, P. Blaha, *Phys. Rev. B,* 65, 033407 (2002);
15. F. Reinert, G. Nicolay, S. Schmidt, D. Ehm, S. Hufner, *Phys. Rev. B* 63, 115415 (2001).
16. R. F. L. Evans, W. J. Fan, P. Chureemart, T. A. Ostler, M. O. A. Ellis, R. W. Chantrell, *J. Phys.: Condens. Matter*, 26, 103202 (2014).
17. W.F. Brown Jr, *IEEE Trans. Magn.* 15, 1196 (1979).
18. H. Yang, O. Boulle, V. Cros, A. Fert, M. Chshiev, *Sci. Rep.*, 8, 12326 (2018).
19. C. Antoniak, J. Lindner, K. Fauth, J.-U. Thiele, J. Minár, S. Mankovsky, H. Ebert, H. Wende, M. Farle, *Phys. Rev. B*, 82, 064403 (2010).
20. S. S. P. Parkin, M. Hayashi, L. Thomas, *Science,* 320, 190 (2008).
21. J. Sampaio, V. Cros, S. Rohart, A. Thiaville, and A. Fert, *Nat. Nanotechnol.,* 8, 839 (2013).
22. F. Greullet, C. Tiusan, F. Montaigne, M. Hehn, D. Halley, O. Bengone, M. Bowen, and W. Weber, *Phys. Rev. Let.* 99, 187202, (2007).